Nano Research

ISSN 1998-0124 CN 11-5974/O4
https://doi.org/10.1007/s12274-024-6972-z

Research Article

Processing of molybdenum industrial waste into sustainable and efficient nanocatalysts for water electrolysis reactions

Federico Ursino[1,2], Giacometta Mineo[1], Antonino Scandurra[1,2,3], Mario Scuderi[4], Angelo Forestan[5], Catya Alba[5], Riccardo Reitano[1], Antonio Terrasi[1,2], and Salvo Mirabella[1,2] (✉)

[1] *Dipartimento di Fisica e Astronomia "Ettore Majorana", Università degli Studi di Catania, via S. Sofia 64, 95123 Catania, Italy*
[2] *CNR-IMM, Università di Catania, via S. Sofia 64, 95123 Catania, Italy*
[3] *Research Unit of the University of Catania, National Interuniversity Consortium of Materials Science and Technology (INSTM-UdR of Catania), Via Santa Sofia 64, 95125 Catania, Italy*
[4] *CNR-IMM, Sede Principale, Strada VIII, 95121 Catania, Italy*
[5] *R & D Spirit Srl-Soc. Unipersonale, Via dei Laghi 67, 36072 Vicenza, Italy*

Received: 2 July 2024 / **Revised:** 1 August 2024 / **Accepted:** 15 August 2024

ABSTRACT

The increasing need for sustainable energy and the transition from a linear to a circular economy pose great challenges to the materials science community. In this view, the chance of producing efficient nanocatalysts for water splitting using industrial waste as starting material is attractive. Here, we report low-cost processes to convert Mo-based industrial waste powder into efficient catalysts for oxygen evolution reaction (OER) and hydrogen evolution reaction (HER). pH controlled hydrothermal processing of Mo-based industrial waste powder leads to pure orthorhombic MoO_3 nanobelts (50–200 nm wide, 10 μm long) with promising OER performances at 10 mA·cm^{-2} with an overpotential of 324 mV and Tafel slope of 45 mV·dec^{-1} in alkaline electrolyte. Indeed, MoS_2/MoO_3 nanostructures were obtained after sulfurization during hydrothermal processes of the MoO_3 nanobelts. HER tests in acidic environment show a promising overpotential of 208 mV at 10 mA·cm^{-2} and a Tafel slope of 94 mV·dec^{-1}. OER and HER performances of nanocatalysts obtained from Mo industrial waste powder are comparable or better than Mo-based nanocatalysts obtained from pure commercial Mo reagent. This work shows the great potential of reusing industrial waste for energy applications, opening a promising road to join waste management and efficient and sustainable nanocatalysts for water splitting.

KEYWORDS

MoO_3, MoS_2, industrial waste, oxygen evolution reaction, hydrogen evolution reaction, critical raw material-free material

1 Introduction

Nowadays, studying new solutions for sustainable energy production is crucial for the development of our society. The decarbonization of industry and other sectors, in particular electricity production, is still challenging also due to the high cost of critical raw materials (CRMs) [1]. Green hydrogen represents a sustainable vector of energy towards green transition. Owing to its versatility and low environmental impact, it can substitute fossil fuels in industry, transportation, aviation and in several chemical and metallurgical industrial processes, thus mitigating the carbon footprint [2]. To date, the hydrogen demand is about 88 Mt per year, but it will increase to 2.3 Gt in the next years, for these reasons the term "hydrogen economy" acquired much interest recently [2].

Green hydrogen can be obtained through water electrolysis powered by electrical energy produced by renewable sources. The water splitting process is based on two different reactions, hydrogen evolution reaction (HER) and oxygen evolution reaction (OER), occurring at the cathode and the anode of an electrolyzer cell, respectively. The best catalysts for HER and OER are Pt and Rh or Ir oxide, respectively [3], which are expensive, rare and at high supply risk, therefore a pressing research goal is finding sustainable and efficient materials to replace them.

Thanks to their multiple oxidation states, transition metal oxides (TMOs) are a promising class of materials for new technologies [4]. Among TMOs there are molybdenum oxides, which possess many features like earth abundance and low cost [5]. Moreover, molybdenum is absent from the CRMs list published in 2023, whereby the use of these elements and their compounds has attracted greater interest [6]. Mo oxides and sulfide are promising electrocatalysts for OER and HER in different electrolyte environment, they are also applied for overall water spitting cell [7–11], still their synthesis can be carried out in many different ways. MoO_2 and MoO_3 are the most diffused molybdenum oxides and the orthorhombic molybdenum trioxide (α-MoO_3) is the most stable phase used for many applications. The molybdenum oxide has a stable structure consisting of a bilayer structure oriented along the [010] direction, which corresponds to the *c*-axis. MoO_3 is a n-type semiconductor, with a bandgap of about 3.0–3.3 eV (depending on the material size and shape) [12–14]. It is used as one-dimensional nanostructures for most applications since this morphology can enhance electrocatalytic performances thanks to the increase of the specific

Address correspondence to salvo.mirabella@dfa.unict.it

surface area [15]. MoO_3 synthesis is widely studied and different procedures were proposed using molybdenum salts as starting reagents [16–18]. For instance, Chen et al. [19] use hydrothermal treatment (HT) to synthesize MoO_3-nanorods, while Xu et al. [20] synthesized MoO_3 nanobelts using a four-step process (calcination–exothermic–hydrothermal treatment–calcination). In both cases the synthesis starts from commercial Mo salts.

Also, transition metal sulphides (TMSs) have attracted much interest in the last decades, like molybdenum disulfide (MoS_2), which was widely studied alone and within different compounds [21]. MoS_2 is usually reported with a few-layered structure, its features and electronic performances strongly depend on the number of layers [22]. Different methods are reported in the literature for the synthesis of MoS_2, for instance, Lai et al. used the chemical vapor deposition (CVD) process to obtain few-layered nanosheets of MoS_2 [10]. Yu et al. use an annihilation process under the flux of argon and H_2, at 450 °C for 1.5 h to synthesize layered crystals of 1T-MoS_2 [23], while Duraisamy et al. used a hydrothermal treatment to obtain nanosheets of MoS_2/MoO_3 starting from commercial MoO_3 powder [11].

The management of waste is another crucial point for the development of our society [24], hence many tests were done to recover materials from waste produced during the development of many devices, like batteries [25]. It was proven that urban mining policies can reduce energy consumption, as described by Shen et al. in their study of some areas of China [26]. Many examples of applications for recycled materials can be found in the literature [27]. In this view, the synthesis of Mo oxide and sulphides starting from industrial waste can be of large interest as sustainable electrocatalysts for hydrogen production. Moreover, the increasing use of Mo in the steel industry, oil and gas industry, corrosion resistance alloys, cast iron and catalyst industries [26] makes it increasingly required and expensive.

Here, we report few-step syntheses of MoO_3 and MoS_2/MoO_3 nanostructures to obtain active electrocatalysts for water splitting starting from Mo-based industrial waste powder. We used low-cost methods and scalable procedures to get nanostructured catalysts with promising HER and OER performances in terms of overpotential, mass activity and Tafel slopes. The reported procedures and results represent a favorable route for industrial waste valorization toward the green energy transition.

2 Materials and methods

2.1 Synthesis of MoO_3 nanobelts

The Mo-based powder precursor, provided by Spirit S.R.L. (Chiampo, Vicenza, Italy), was obtained after thermal treatments (in a muffle, 700 °C for 3 h) of metal industrial waste and it was commercially denominated as recycled P-MOOX. Here, we use a two-step synthesis to obtain the MoO_3 nanobelts. Firstly, an exothermic reaction between recycled Mo-based powder (labelled as R0) and hydrogen peroxide (H_2O_2, 30 wt.%, Sigma Aldrich) occurred, mixing 0.5 g of R0 powder with different amounts of H_2O_2 as reported in Table 1. The ratio of H_2O_2 mass to that of R0 powder gives the name to the sample, as described in Table 1, so that N18 describes a solution of 10 mL H_2O_2 with 0.5 g of R0 powder. The obtained peroxo-molybdic acid solution was magnetically stirred for 30 min, after that the solution pH was measured. The second step was the HT: the obtained peroxo-molybdic acid solution was transferred into a Teflon liner and deionized water was added to obtain a volume of 25 mL. The liner, put into an autoclave, was inserted in a muffle for 3 h at 180 °C, after which the solution was left to cool to room temperature for 18 h. The resulting solution was centrifuged (6000 rpm for 10 min), washed with ethanol and deionized water and dried on a hot plate (75 °C for 45 min) to obtain the dried MoO_3 nanobelts powder.

Table 1 MoO_3 nanobelt synthesis summary. The mass of the starting Mo-based powder (R0) was fixed to 0.5 g

Name	H_2O_2 (mL)	H_2O_2:R0	pH
N18	9.0	18	1.26
N14	7.0	14	1.35
N7	3.5	7	1.60
N0	0	0	2.35

2.2 Synthesis of MoS_2/MoO_3 nanostructures

MoO_3-nanobelts powder, obtained as described above, was employed for the synthesis of MoS_2/MoO_3 nanostructures. MoO_3-nanobelts powder (22 mg of N18 sample) was magnetically stirred for 30 min with different amounts of thiourea (TU, by Sigma Aldrich) and 15 mL of deionized water (see Table 2 for details). The molar ratio of TU to MoO_3 powder gives the name to the sample, so that SN7 describes a solution of 80 mg TU with 22 g of MoO_3-nanobelts powder. Once stirred, the solution was transferred into the Teflon liner, inserted in an autoclave and placed in a muffle for 3 h at 180 °C. The autoclave was then cooled at room temperature for 18 h and the obtained product was centrifuged and washed with water and ethanol at 6000 rpm for 30 min. The resulting solution was concentrated at 100 °C under nitrogen flux for about 4 h. To assess the effect of the two-step synthesis of MoO_3-nanobelts, one synthesis, called SR5.0, was performed using R0 as precursor in place of MoO_3-nanobelts powder.

2.3 Preparation of the electrodes

OER and HER electrodes were prepared by applying the powder of MoO_3-nanobelts and MoS_2/MoO_3 nanostructured electrocatalysts onto graphene paper (GP, Sigma Aldrich, 240 μm thick), which was used as substrate. In detail, 1 mg of nanobelts powder was dispersed in 1 mL of deionized water and a solution of polyvinylidene difluoride (PVDF, Sigma Aldrich, 50 μL) in acetone (11 $g{\cdot}L^{-1}$) was added. The mixture was sonicated for 30 min. The PVDF is used as a binder and does not influence the performance of the material, as reported in the literature [28]. The mixture was drop-casted on a GP substrate and dried at room temperature for one night. The deposited mass was calculated as the difference between the electrode mass after and before the drop-casting and drying steps, by using a Mettler Toledo MX5 Microbalance with a sensitivity of 0.01 mg. The area of the exposed mass was measured for each sample, thus obtaining a mass loading of 0.9 $mg{\cdot}cm^{-2}$ for MoO_3-nanobelts. MoS_2/MoO_3 nanostructures were directly dropped cast on GP substrate without any binder, with a catalyst loading of about 3 $mg{\cdot}cm^{-2}$.

2.4 Characterization techniques

The morphology of the samples was studied using a scanning electron microscopy (SEM) Gemini Field Emission SEM Carl Zeiss SUPRATM 25 (FEG-SEM, Carl Zeiss Microscopy GmbH, Jena, Germany) set to the in-lens mode. The X-ray diffraction (XRD) pattern was acquired with a Bruker-AXSD5005θ-θ diffractometer, with a gobel mirror to parallel the Cu Kα radiation operating 40 kV at 30 mA.

Table 2 MoS_2/MoO_3 nanostructures synthesis summary

Name	Molybdenum based powder (mg)	TU (mg)	TU/MoO_3 (molar ratio)
SN2.5	22 (N18)	34	2.5
SN5.0	22 (N18)	57	5.0
SR5.0	22 (R0)	57	5.0
SN7.0	22 (N18)	80	7.0

The transmittance measurements were performed using a PerkinElmer UV/Vis/NIR Spectrometer Lambda 1050+ between 250 and 800 nm, with steps equal to 2 nm (UV: ultraviolet, Vis: visible and NIR: near-infrared). The Raman spectra were recorded through a Horiba Scientific instruments model 1024X256-OE, with a laser by THORLABS model HNL225R with a wavelength of 633 nm.

The presence of Mo, O and S in the synthesized materials was evaluated by Rutherford backscattering spectrometry (RBS), using a 2.0 MeV He^+ beam at normal angle incidence, accelerated by a 3.5 MV High Voltage Engineering Europa (HVEE) Singletron accelerator system. RBS was performed by collecting backscattered ions at 165° off the axis and spectra were analyzed using XRump software (Thompson M., Windows (95-Win7)-Genplot and RUMP, available online, http://www.genplot.com/download.htm).

The as-synthesized nanostructures were transferred from the substrate directly on the transmission electron microscopy (TEM) grid for TEM characterization by mechanical rubbing. The obtained specimens were examined using a Cs-probe-corrected TEM JEOL ARM200CF microscopy, operated at 200 keV in scanning-TEM (STEM) mode.

The electrochemical measurements were performed using a potentiostat (model VersaSTAT 4, Princeton Applied Research, USA) with a three-electrodes setup. OER measurements were performed in an alkaline electrolyte (1 M KOH), while for HER an acidic media was employed (1 M H_2SO_4). Saturated calomel electrode (SCE) was used as reference electrodes, the counter electrodes were Pt wire and graphite rod, for OER and HER, respectively. The electrodes prepared with Mo-based nanostructures were used as working electrodes. The electrochemical performances of the Mo-based nanostructures were measured by linear sweep voltammetry (LSV), with a scan rate of 5 $mV \cdot s^{-1}$ from 0 to 1.7 V and from 0 to −1 V vs. SCE for OER and HER analysis, respectively. The measured potential was converted from SCE to reversible hydrogen electrode (RHE) using the Nernst equation [29]

$$E_{RHE} = 0.241\ V + E_{SCE} \times pH \times 0.059 \quad (1)$$

where E_{RHE} is the potential vs. RHE, 0.241 V is the standard potential of SCE at 25 °C and E_{SCE} is the measured potential vs. SCE. Tafel analysis was obtained from the LSV measurements. Electrochemical impedance spectroscopy (EIS) analysis was carried out in a potentiostatic mode. An alternating current (AC) voltage with an amplitude of 10 mV and frequency that varies from 100 kHz and 10 mHz is superimposed to a constant voltage (which is fixed at the potential at 10 $mA \cdot cm^{-2}$). The uncompensated resistance R_u extracted from EIS curves was used to correct the potential as follows [30]

$$E_{RHE}^{corr} = E_{RHE} - iR_u \quad (2)$$

in which i is the measured current (A) and E_{RHE}^{corr} is the corrected potential.

3 Morphological and phase characterization

3.1 MoO_3 nanobelts

XRD (Fig. 1(a)) pattern of R0 shows that it is mostly composed of a mixture of metallic molybdenum (peaks at 40.56° and 58.76°, labelled with M, card No. 00-089-5023) and molybdenum dioxide (peaks at 26.06°, 36.88° and 53.60°, labelled with asterisk, card No. 00-076-1807). This result was also confirmed by RBS (see Fig. S1(a) in the Electronic Supplementary Material (ESM)) measurement, which shows a ratio between the doses of O and Mo of 2, well smaller than that expected for molybdenum trioxide. Basing on these results, during the first step of MoO_3 nanobelts synthesis, different exothermic reactions may occur leading to several peroxo-molybdate species [31, 32]. The peroxo-molybdate

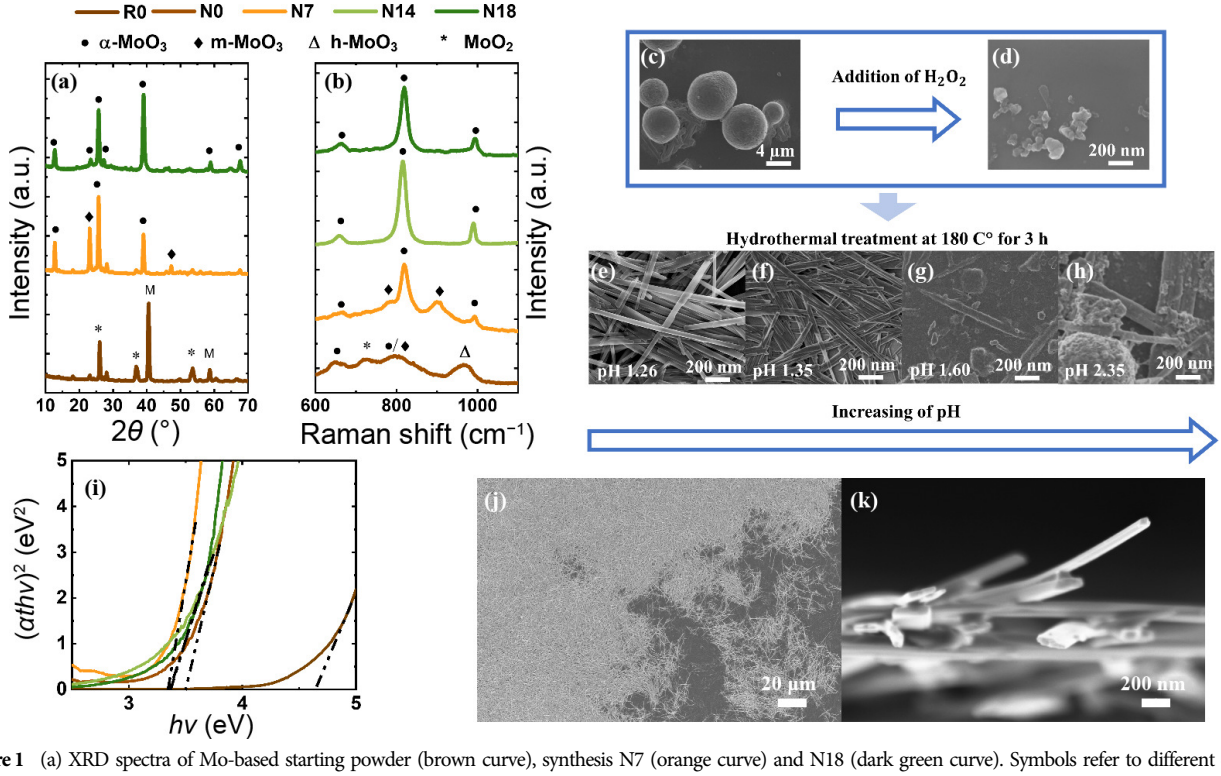

Figure 1 (a) XRD spectra of Mo-based starting powder (brown curve), synthesis N7 (orange curve) and N18 (dark green curve). Symbols refer to different crystal phase reflections, while "M" stands for metallic Mo reflections. (b) Raman spectra of nanobelts prepared at pH 2.35 (light brown curve), pH 1.60 (orange curve), pH 1.35 (light green curve), pH 1.26 (dark green curve). SEM images of: (c) Mo-based powder (R0); (d) powder extracted by the peroxo-molybdic solution after the exothermic reaction with 5 mL of H_2O_2; (e)–(h) powders obtained after the hydrothermal treatments conducted by using the pH 1.26 (N18), the pH 1.35 (N14), the pH 1.60 (N7) and the pH 2.35 N0 synthesis, respectively. The scale bar is 200 nm for panels c to h. (i) Tauc plot for the MoO_3 nanostructures synthesis and Mo-based starting powder. SEM images of N18 sample at (j) low magnification and (k) in cross view.

species are generally unstable and evolve into molybdic acid and then, into MoO_3 nanobelts. Thus, to describe the initial stage of the synthesis we can consider the resulting equations [33, 34]

$$xH_2O_2 + MoO_{(3-x)} \rightarrow H_2MoO_4 + (x-1)H_2O \quad (3)$$

$$H_2MoO_4 \rightarrow MoO_3\,(\text{nanobelts}) + H_2O \quad (4)$$

The effect of hydrogen peroxide during the process was tested by varying the amount of H_2O_2 during the synthesis (Table 1). Each synthesis procedure is labelled thus taking into consideration the H_2O_2 added amount. The N0 sample was obtained without any H_2O_2 addition, by using R0 dispersed in deionized water as a precursor (no exothermic reactions occurred).

In Fig. 1(a) the XRD patterns of two MoO_3 nanobelt samples (N7 and N18) are reported, together with that of the starting Mo-based powder (R0), for comparison. The N7 sample shows a clear MoO_3 crystal structure, even if two different phases are present: orthorhombic MoO_3 (12.76°, 25.74° and 39.04° 2θ peaks, labelled with a full circle, card No. 00-005-0508) and monoclinic MoO_3 (23.1° and 47.28° 2θ peaks, labelled with a full rhombus, card No. 00-047-1320). This confirms the possibility to have a coexistence of α-MoO_3 and m-MoO_3, as expected [35]. N18 sample presents XRD peaks linked only to orthorhombic MoO_3 (12.76°, 23.42°, 25.76°, 27.3°, 39.02° and 58.9° 2θ peaks, labelled with a full circle). For the orthorhombic phase of N7 and N18 the most intense peaks are referred to (0*k*0) growth direction, that is the preferential nanobelts growth direction, which is a consequence of surface energy modification along the other directions [18]. Thus, suggesting that the high concentration of H^+ ions in solution, confirmed by the very low pH values recorded, helps to saturate the dangling bonds along (00*h*) and (*m*00) directions.

Figure 1(b) shows the Raman spectra of four MoO_3 samples (N0, N7, N14 and N18). N0 sample shows rough peaks at 649, 722, 803 and 968 cm^{-1}, pointing to the presence of MoO_2 (labelled with asterisk), α-MoO_3 (labelled with a full circle) and m-MoO_3 (labelled with an full rhombus) [36]. N7, N14 and N18 samples show more evident peaks, at 663, 819 and 991 cm^{-1}, related to α-MoO_3 [19], which is the most stable phase of the molybdenum trioxide. It should be noted that N7 spectrum shows two further peaks at 778 and 904 cm^{-1} [35], characteristic of m-MoO_3, thus confirming XRD analysis. These results suggest that for our synthesis a low pH value is beneficial for obtaining a pure α-MoO_3 crystal phase, probably due to the large abundance of H^+ ions favoring the reaction of peroxo-molybdate species according to Eqs. (3) and (4).

RBS analysis was carried out on N18 samples to estimate the chemical composition and the stoichiometry (see Fig. S1(b) in the ESM). The RBS spectrum shows a Mo to O atomic ratio close to 1:3, confirming a chemical composition fully compatible with MoO_3 (see the details of the analysis in the ESM).

To study the role of the pH in the morphology of the obtained nanostructures, SEM imaging is used and the obtained data are reported in Figs. 1(c)–1(h). The morphology largely changes due to different pH values during the synthesis. R0 is made of spheres with an average diameter of 5 μm (Fig. 1(c)) which break up with the addition of 5 mL of H_2O_2, as suggested by SEM image in Fig. 1(d). Figures 1(e)–1(h) show the nanostructures present in the N0, N7, N14 and N18 samples, after the HT step. We can see the presence of elongated structures (50–100 nm in section, several μm in length, called nanobelts), nanospheres and debris. By increasing the H_2O_2 amount the presence of the spheres decreases with the pH and at more acidic pH values only nanobelts are present, thus confirming the beneficial role of H^+ ions in the conversion of peroxo-molybdic acid into orthorhombic MoO_3.

The optical bandgap of our MoO_3 nanobelts was estimated by dispersing them in deionized water and measuring the transmitted light intensity. The product αt was calculated using the Beer–Lambert law [37]

$$\alpha t = \ln\left(\frac{1}{T}\right) \quad (5)$$

where α is the absorption coefficient, t is the equivalent thickness of nanostructures and T is the recorded transmittance. Figure 1(i) reports the Tauc plots of $(\alpha t h\nu)^{1/n}$ as a function of photon energy, $h\nu$, with n = 1/2 because we assume that the samples have direct bandgap transitions [38]. The extrapolated intercept with the *x*-axis gives an estimation of the optical bandgap. The calculated values were reported in Table S1 in the ESM. For N7, N14 and N18, the optical bandgap is about 3.3 eV, which is in good agreement with that of bulk α-MoO_3 [12, 14], while for N0 it is equal to 3.5 eV, as expected considering that MoO_2 bandgap value reported in the literature is a bit higher than that of α-MoO_3 [36]. R0 reports an optical bandgap of 4.3 eV linked to pure MoO_2 [36]. The optical bandgap values decrease with the pH, hence these estimations further confirm the effect of hydrogen peroxide on the stoichiometric composition of nanostructures through the different syntheses.

The data shown so far confirm the effectiveness of our low-cost synthesis route for the transformation of the starting Mo-based powder into MoO_3 nanostructures with a defined shape, size, crystal structure and optical band gap and that a pH lower than 1.60 is needed to obtain stoichiometric MoO_3 nanobelts. Indeed, low-magnification SEM images of N18 (Fig. 1(j)) reveals the abundant presence of nanobelts all over the sample; a cross-section SEM image (Fig. 1(k)) demonstrates the very narrow width and thickness (about 200 and 50 nm, respectively) of nanobelts.

3.2 MoS_2/MoO_3 nanostructures

The synthesis of MoS_2/MoO_3 nanostructures is based on the α-MoO_3 nanobelts powder (N18 sample) described above. Thiourea was added to MoO_3 powder with different volume ratios (see Table 2), magnetically stirred and used for the HT step. Each sample is labelled with the TU to MoO_3 nanobelts molar ratio. To evidence the advantage of starting with MoO_3 nanobelts, a synthesis (SR5.0 sample) was done using the R0 as a precursor.

Figure 2(a) shows the XRD spectra of different samples. As well known, the nanometric size of our materials affects the peaks, producing shifts and broadening [39]. SN2.5, SN5.0, SN7.0 and SR5.0 samples show a peak at 14° (green vertical band) which can be linked to (002) plane of 2H-MoS_2. Only SN5.0 sample reports also the other expected peaks at 40° and 57° (green vertical bands), related to (103) and (110) planes of 2H-MoS_2, respectively [11, 39, 40–42]. Other peaks were recorded, like those around 12° and 52°, which are assigned to α-MoO_3 (card No. 00-005-0508). The presence of MoO_2 can be suggested by the peaks at 19°, 37° and 57° (card No. 00-076-1807). According to XRD patterns, the treatment in HT with TU modifies the α-MoO_3 nanobelts by reducing it and adding MoS_2 phases, as expected.

Figure 2(b) reports the Raman spectra of the samples, which show Mo–S bond peaks, at around 370 and 405 cm^{-1} (E_{2g}^1 in-plane and A_{1g} out-plane phonon modes, respectively, highlighted in the green region) [43]. SN2.5 sample does not present defined peaks, this suggests that only a few numbers of Mo–S bonds were formed. The $\Delta\kappa$ difference between E_{2g}^1 and A_{1g} peaks is an important datum, since in MoS materials the interlayer distance among MoS_2 planes increases when $\Delta\kappa$ decreases [44]. In this work increasing TU ratio $\Delta\kappa$ decreases, 38 and 30 cm^{-1}, respectively for SN5.0 and SN7.0. According to the literature, the low difference between these two peaks can be related to a few-layered structure, as recorded in the last two samples [44]. SN2.5

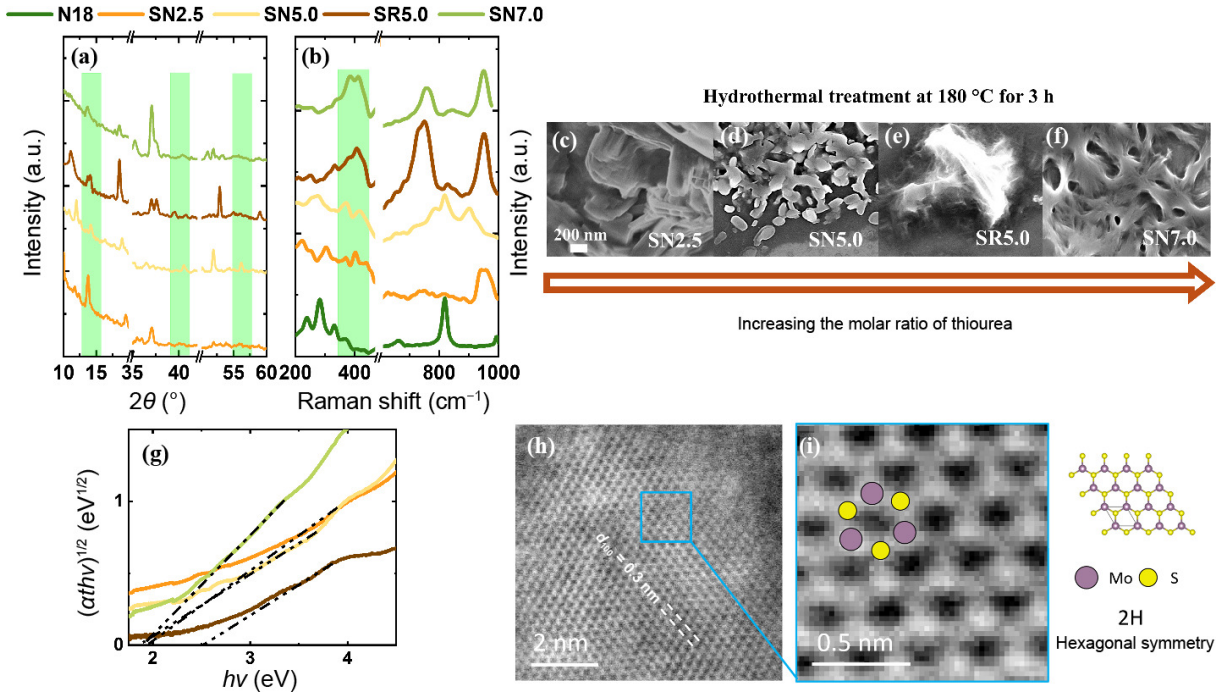

Figure 2 (a) XRD spectra of SN2.5 (orange curve), SN5.0 (yellow curve), SN7.0 (dark yellow curve) and SR5.0 (brown curve). (b) Raman spectra of different samples are also reported compared with N18 (dark green curve). SEM image of samples with different TU/MoO_3 molar ratio: (c) SN2.5, (d) SN5.0, (e) SR5.0 and (f) SN7.0. (g) Tauc plots for different samples with the linear fit to extract the optical bandgap. (h) High-resolution STEM Z-contrast image of the 2H-MoS_2. (i) Zoom-in of the of the area marked by the blue square, showing the positions of the atoms alongside the atomic model of 2H-MoS_2.

and SN5.0 samples still report broadened peaks between 270 and 330 cm^{-1}, which can be attributed to the presence of large amounts of molybdenum oxide [19]. SN2.5 has a defined peak around 950 cm^{-1} assigned to $MoO_3 \cdot 2H_2O$ [45], also SN7.0 reports this peak together with one at 760 cm^{-1} which can be a convolution between MoO_2 (743 cm^{-1} [36]) and $MoO_3 \cdot H_2O$ (776 cm^{-1} [45]), while SN5.0 is characterized by monoclinic (786 and 903 cm^{-1} [35]) and orthorhombic (660 and 820 cm^{-1} [19]) peaks. The different widths of the peaks can be attributed to the effect of the boundaries, according to the presence of nanostructured material [46]. Raman spectra highlight the presence of Mo–S and Mo–O bonds compatible with MoS_2, MoO_3 and MoO_2, confirming XRD conclusions.

SEM analysis shown in Figs. 2(c)–2(f) demonstrates that by increasing TU, the size and shape of obtained nanostructures change. SN2.5 SEM image (Fig. 2(c)) could give a hint of the nanobelt fragmentation and SEM image of SN5.0 (obtained by increasing TU/MoO_3) shows the presence of irregular debris (Fig. 2(d)), with a side of about 300 nm. Figure 2(e) reports the SR5.0 sample, in which, despite the use of the same molar ratio of SN5.0, very thin irregular structures are present. This points out the importance of using a MoO_3 nanobelts powder in place of the R0 powder. At well higher TU/MoO_3 ratio (SN7.0) irregular structures aggregate in a jagged network (Fig. 2(f)). The addition of TU activates the sulfurization of Mo oxide powder, leading to a fragmentation of original nanobelts. A smaller amount of TU probably affects only the surface of the starting powder, leaving traces of the nanobelts, while a too-large TU destroys every memory of the nanobelts. It seems that a medium TU amount can give the best results as the MoS_2 formation is concerned.

The absorption coefficient was calculated using Eq. (5) and the Tauc plots (see Fig. 2(g)) were produced by $(\alpha h\nu)^{1/n}$, with $n = 2$ since molybdenum disulphide is considered an indirect bandgap material [22]. Tauc plots of SN2.5, SN5.0 and SN7.0 samples show optical bandgaps around 1.8 eV, higher than of pure MoS_2, which is around 1.2 eV [22]. SR5.0 sample shows a very different value (2.5 eV) from other syntheses. These results suggest that the treatments started from nanostructured materials produce nanostructures closer to MoS_2 than the synthesis obtained starting from Mo-based powder.

Other characterizations were performed on the SN5.0 synthesis due to the presence of tiny structures, indeed it was also studied the RBS spectrum (see Fig. S2 in the ESM), showing the presence of molybdenum at 1.7 MeV, oxygen and sulphur at 0.7 and 1.2 MeV. High-resolution STEM images taken on structures from SN5.0 synthesis show the crystal lattice typical of 2H-MoS_2 phase (see Figs. 2(h) and 2(i)).

These characterizations confirm that the HT process with TU performed on the N18 powder leads to different Mo-based phases and morphologies, probably related to a mixture of molybdenum sulphide and oxides (MoS_2 and MoO_3).

4 Electrochemical characterization

4.1 OER electrocatalysts

The electrochemical OER performances of MoO_3 nanobelts were studied by LSV, as reported in Fig. 3(a), after the *iR* correction. The curves of bare GP and Mo-based starting powder (light blue and dark brown curves, respectively) are also reported to evidence the substrate and nanostructures' presence effect. After an initial plateau, in which no current flows between the electrodes, the OER mechanism starts and the current rapidly increases with the potential increase, with features that depend on the morphology, crystallinity and stoichiometry of MoO_3 nanostructures. To compare the efficiency of all the electrodes, the overpotential at 10 $mA \cdot cm^{-2}$ was extracted from LSV curves and reported in Table S1 in the ESM. It should be noted that the Mo-based catalyst amount is 0.9 $mg \cdot cm^{-2}$ for all the samples. The lowest overpotential is obtained for N18 sample (324 mV, dark green curve), well lower than that of the GP substrate and Mo-based starting powder (360 and 340 mV, respectively). For the N0 sample (light brown curve) a promising overpotential (326 mV) is obtained, then, by reducing the pH, the overpotential increases until it reaches 362 mV for the N7 and then decreases, reaching the minimum overpotential (324 mV) for N18 sample. Raman analysis (Fig. 1(b)) shows the presence of sub-stoichiometric

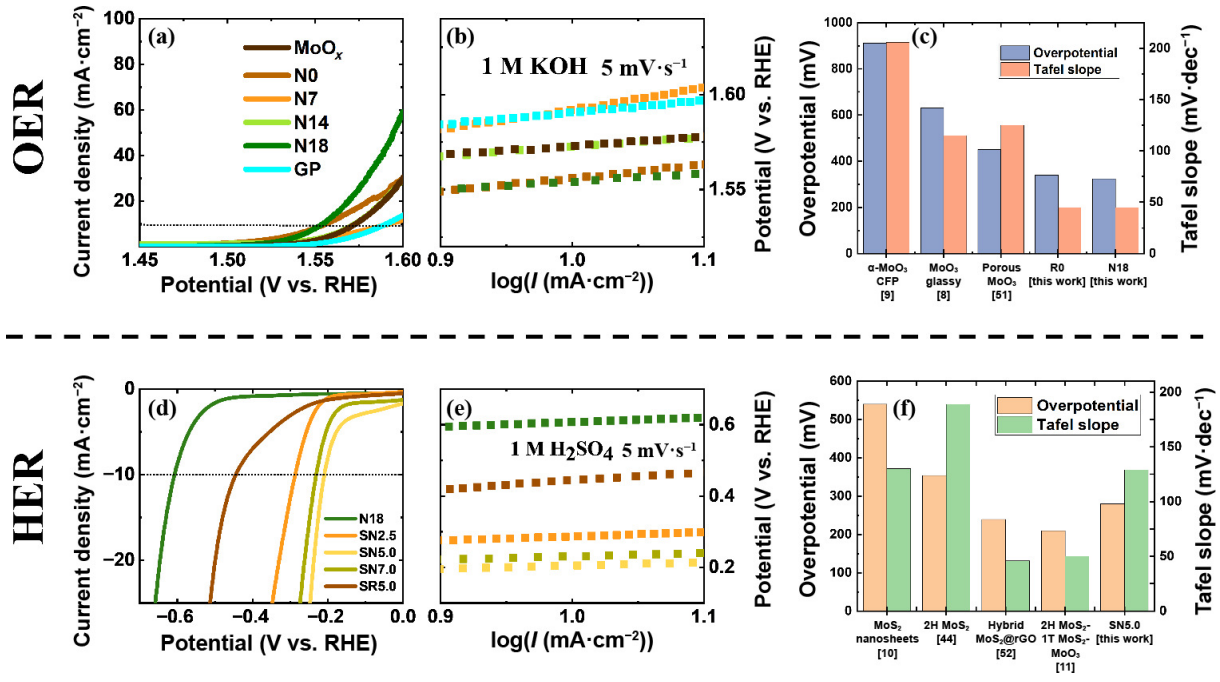

Figure 3 (a) LSV curves after *iR* correction using EIS measurements (Fig. S3 in the ESM) and (b) Tafel slopes of synthesis N0 (light brown curve), N7 (orange curve), N14 (light green curve) and N18 (dark green curve) compared to graphene paper (light blue curve) and Mo-based powder (dark brown curve). The measurements were done in 1 M KOH. (c) MoO_3-nanobelts are compared with similar MoO_3-based catalysts active for OER application. (d) LSV curves of MoO_3 nanobelts (N18, dark green curve) compared with SN2.5 (orange), SN5.0 (light orange curve), SN7.0 (dark yellow curve) and SR5.0 (yellow curve) in 1 M H_2SO_4; (e) Tafel plot of the different samples. The overpotentials was calculated at 10 mA·cm^{-2}. (f) MoS_2/MoO_3-nanostructures are compared with MoS_2-based catalysts active for HER application in 0.5 M H_2SO_4.

molybdenum oxides characterized by oxygen vacancies, these defects can lead to better OER performances, as just reported in the literature [37]. Then, when the stoichiometric structure is obtained (N7 and N18 samples), the OER performances depend on the morphology and crystallinity, reaching the best response for the N18 sample (only α-MoO_3).

Tafel analysis was carried out to determine the Tafel slope which allows us to achieve a deeper knowledge of the charge transport mechanism involved during the OER process [47]. In Fig. 3(b), the Tafel plots for the different syntheses are displayed, with a magnification around 10 mA·cm^{-2}; the lower Tafel slope belongs to N18 and N14 samples, which are 45 and 50 mV·dec^{-1}, respectively, while N7 and N0 have higher values, as reported in Table S1 in the ESM. While N18 and N0 samples show similar low overpotential, they possess quite different Tafel slopes, highlighting a different OER kinetics. N18 sample has by far a lower Tafel slope, leading to an outperformance at a higher current. The band position of MoO_3 is favourable for OER application, but also the nanobelt growth along (0*k*0) produces many edge sites along other directions and these can act as active sites for the adsorption mechanism of OH–, justifying the lower Tafel slope reported for N18. On the other hand, higher values of Tafel slopes are accounted to a predominance of recombination mechanism at the surface, as reported in literature [47]. N18 shows the best performances for OER, hence we decided to test its durability as shown in Fig. S6 in the ESM (green curve). The sample shows excellent stability for 15 h. In Fig. 3(c), the overpotential and Tafel slope of N18 and R0 samples are compared with literature data of MoO_3-based catalysts for alkaline OER (see Table 3). A remarkable improvement of both overpotential and Tafel slope respect to the literature data is evident, despite the use of industrial waste powder as starting material.

The electrocatalytic activity of the samples has been verified by calculating the mass activity at 10 mA·cm^{-2}, which is a useful estimation of the intrinsic activity of electrocatalysts (see Table S1 in the ESM). The mass activity can be calculated with the relation [48, 49]

$$\text{Mass activity} = \frac{J}{m_{\text{loaded}}} \tag{6}$$

where J is the current density expressed in A·cm^{-2} and m_{loaded} the deposited mass load of each electrode in mg·cm^{-2}. For N18, N14 and N7 samples the mass activity at 10 mA·cm^{-2} is around 1.2 × 10^{-2}–1.3 × 10^{-2} A·mg^{-1}. The N0 and R0 mass activity (1.0 × 10^{-2} A·mg^{-1}) are lower than the previous ones. These values are comparable with those present in literature, as reported in Table 3.

4.2 HER electrocatalysts

The electrochemical characterization of MoS_2/MoO_3 as HER electrocatalysts can be appreciated from LSV curves reported in Fig. 3(d), after *iR* correction. The N18 (dark green curve) is shown to highlight the beneficial effect of sulfurization. All the measurements are characterized by an initial plateau followed by

Table 3 Comparison of catalytic parameters of MoO_3-based materials, at 10 mA·cm^{-2} with 1 M KOH electrolyte

Catalyst	Overpotential (η (mV))	Tafel slope (mV·dec^{-1})	Mass activity (10^{-2} A·mg^{-1})	Catalyst loading (mg)	References
α-MoO_3/carbon fiber paper (CFP)	910	206	1.00	0.10	[8]
MoO_3/glassy carbon	630	115	5.0	0.04	[7]
Porous MoO_3	450	125	5.0	1.40	[50]
Mo-based powder (R0)	340	45	1.0	1.00	This work
MoO_3-nanobelts (N18)	324	45	1.2	0.80	This work

the HER onset. In Table S2 in the ESM the electrochemical parameters of the samples are resumed, focusing on 10 and 25 mA·cm^{-2}. The N18 show a very high overpotential at 10 mA·cm^{-2} (608 mV), followed by SR5.0 sample (444 mV). SN2.5 and SN5.0 samples show a significant decrease of the overpotential (290 and 205 mV, respectively), while it slightly increases with SN7.0 sample (230 mV).

Figure 3(e) shows the Tafel plots for the different syntheses. The lowest Tafel slope was obtained for SN7.0 (91 mV·dec^{-1}) and SN5.0 (94 mV·dec^{-1}), while for SN2.5 it is 117 mV·dec^{-1}. The Tafel slopes reflect the slowest mechanism that occurs during HER and for these samples the Tafel slope values can be accounted to a Volmer step as rate determining step (RDS) [47]. The trend of performances at 25 mA·cm^{-2} is the same observed at lower current density and SN5.0 is still the best sample. At 25 mA·cm^{-2} SN5.0 records an overpotential two times lower than SR5.0.

For all the samples, the electrocatalytic activity was also evaluated through the mass activity estimate, for both 10 and 25 mA·cm^{-2}. For instance, the mass activity values were reported in Table S2 in the ESM, SN5.0 shows mass activity values of 0.3 × 10^{-2} A·mg^{-1}, 0.8 × 10^{-2} A·mg^{-1}, respectively at 10 and 25 mA·cm^{-2}. SN5.0 was also measured for long-term stabilization measurements, showing a fair stability for 15 h (see Fig. S6 in the ESM, orange curve).

SN5.0 was also measured in 0.5 M H_2SO_4, an overpotential of 280 mV and a Tafel slope of 129 mV·dec^{-1} were evaluated from LSV curve (see Fig. S5 in the ESM). As just said, molybdenum disulfide was widely treated in the literature, this fact allows us to compare our results with the state-of-the-art, as reported in Fig. 3(f) (see Table 4 for details). It is possible to observe how our sample possesses a lower overpotential than pure MoS_2 [43] and other alloys. SN5.0 sample was obtained after a sulfurization of MoO_3; actually the bandgap of MoS_2 is smaller than that of MoO_3, according to literature [21] and shown by optical band gap calculations and moreover the conduction band is closer to the H^+/H_2 level for water splitting, representing a great advantage for HER. Hence, thanks to band position more electrons are available for HER than MoO_3 case.

At the best of our knowledge, there are no works that deal with nanostructures obtained by recycled powder. Hence this work opens a new path for the employment of industrial waste and the production of sustainable nanocatalysts.

4.3 Overall water splitting (OWS) cell

As proved, the synthesized electrocatalysts MoO_3 and MoS_2/MoO_3 are active for OER and HER, respectively. The alkaline electrolyte is a promising choice for OWS cell application according to the literature [52, 53] so we characterized the SN5.0 sample in alkaline electrolyte (1 M KOH). In Fig. 4(a) the LSV curve of SN5.0 is reported, with a promising overpotential of 370 mV in alkaline electrolyte (1 M KOH), it was evaluated also the Tafel slope of 43 at 10 mV·dec^{-1} (Fig. S5(a) in the ESM). After this characterization the OWS was assembled as reported in Fig. 4(b). The sample N18 based on MoO_3 was employed as anode, while SN5.0 one is used as cathode in alkaline electrolyte 1 M KOH. The resulted OWS cell shows a potential of about 1.9 V (see Fig. 4(c)) and a Tafel slope of 57 mV·dec^{-1} (Fig. S5(c) in the ESM).

5 Conclusions

In this work recycled material is valued, as it is processed using a low-cost method, into efficient and sustainable nanocatalysts active for OER and HER reactions, opening the way to join energy needs and waste management.

Starting from Mo-based powder obtained from industrial waste, α-MoO_3 nanobelts (50–200 nm wide, 10 μm long) were obtained by pH-controlled hydrothermal synthesis (180 °C, 3 h). Higher pH values lead to mixed crystal phases or substoichiometric oxides. α-MoO_3 nanobelts produced at acidic pH showed promising OER features in alkaline conditions (overpotential of 324 mV, Tafel slope of 45 mV·dec^{-1} and mass activity of 1.2 × 10^{-2} A·mg^{-1}, at 10 mA·cm^{-2}). It should be noted that our α-MoO_3 nanobelts, produced by recycled industrial waste, display catalyst performances higher than other Mo oxide-based catalysts present in the literature.

To produce effective HER electrocatalysts we developed a hydrothermal synthesis in thiourea solution, to reduce and sulfurize the α-MoO_3 nanobelts obtained above. Actually, by optimizing the thiourea/nanobelts ratio, a mixture of molybdenum sulphide and oxides (MoO_3 and MoO_2) is achieved with irregular nanostructures debris (100–300 nm in size). The best HER performances in acidic condition (overpotential of 208 mV, Tafel slope of 94 mV·dec^{-1} and mass activity of 0.3 × 10^{-2} A·mg^{-1}, at 10 mA·cm^{-2}) were found to be comparable or better than literature data with Mo-based catalysts with similar composition.

A OWS cell was successfully tested in alkaline electrolye, showing a potential of 1.9 V and a Tafel slope of 57 mV·dec^{-1}, nevertheless the potential higher than the literature this test is a good starting point for future projects [53].

Hence, these data show a sustainable route to synthesize efficient OER and HER nanocatalysts using recycled industrial waste powder, that is a key element for low-impact solutions for energy production.

Acknowledgements

This work has been partially funded by European Society (Next Generation, EU), through the MUR-PNRR project PRIN IMAGE (No. P2022KACL7). The authors thank the Bio-nanotech Research and Innovation Tower (BRIT) laboratory of the University of Catania (No. PONa3_00136 financed by the MIUR) for the Smartlab diffractometer facility and Professor G. Malandrino (University of Catania) for discussion and experimental XRD analysis. Part of the experiments was carried out using the facilities of the Italian Infrastructure Beyond Nano.

Table 4 Comparison of catalytic parameters of MoS_2-based materials, at 10 mA·cm^{-2} in 0.5 M H_2SO_4 electrolyte

Catalyst	Overpotential (mV)	Tavel slope (mV·dec^{-1})	Mass activity (10^{-2} A·mg^{-1} @10 mA·cm^{-2})	Catalyst loading (mg·cm^{-2})	References
Few-layered MoS_2 nanosheets	540	130	0.3	3.57	[10]
2H MoS_2	354	189	0.3	3.00	[43]
MoS_2@reduced graphene oxide (rGO) hybrid	239	46	2.5	0.40	[51]
2H MoS_2-1T MoS_2-MoO_3	210	50	3.5	0.28	[11]
2H MoS_2-MoO_3	280	129	0.28	3.60	This work

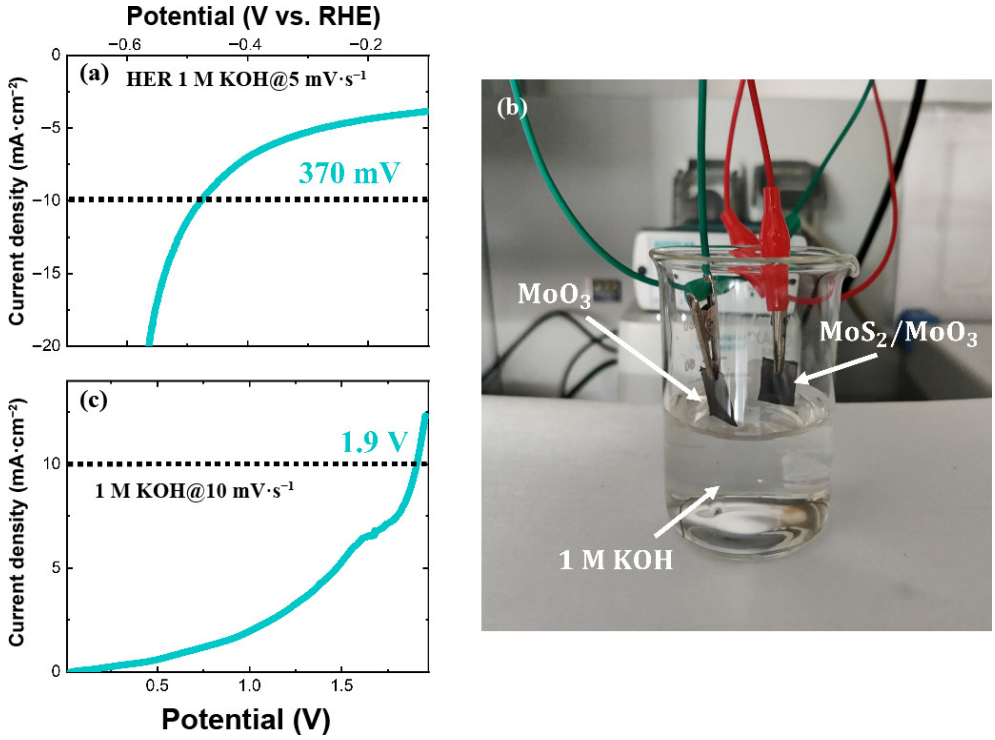

Figure 4 (a) LSV curve of SN5.0 sample in 1 M KOH with a scan rate of 5 mV·s^{-1}, an overpotential of 370 mV is reported; (b) LSV curve of the OWS cell composed by MoO_3 (anode) and MoS_2/MoO_3 (cathode); (c) the used setup for the measurements on the OWS cell.

Funding note: Open access funding provided by Università degli Studi di Catania within the CRUI-CARE Agreement.

Electronic Supplementary Material: Supplementary material (RBS analysis, EIS measurements and further synoptic table) is available in the online version of this article at https://doi.org/10.1007/s12274-024-6972-z.

References

[1] Wei, M.; McMillan, C. A.; De La Rue Du Can, S. Electrification of industry: Potential, challenges and outlook. *Curr. Sustain. Renew. Energy Rep.* **2019**, *6*, 140–148.

[2] Oliveira, A. M.; Beswick, R. R.; Yan, Y. S. A green hydrogen economy for a renewable energy society. *Curr. Opin. Chem. Eng.* **2021**, *33*, 100701.

[3] Leal Filho, W.; Kotter, R.; Özuyar, P. G.; Abubakar, I. R.; Eustachio, J. H. P. P.; Matandirotya, N. R. Understanding rare earth elements as critical raw materials. *Sustainability* **2023**, *15*, 1919.

[4] Agnihotri, A. S.; Varghese, A.; Nidhin, M. Transition metal oxides in electrochemical and bio sensing: A state-of-art review. *Appl. Surf. Sci. Adv.* **2021**, *4*, 100072.

[5] De Castro, I. A.; Datta, R. S.; Ou, J. Z.; Castellanos-Gomez, A.; Sriram, S.; Daeneke, T.; Kalantar-Zadeh, K. Molybdenum oxides-from fundamentals to functionality. *Adv. Mater.* **2017**, *29*, 1701619.

[6] European Commission. *RMIS—Raw Materials Information System* [Online]. https://rmis.jrc.ec.europa.eu/ (accessed Sep 4, 2024).

[7] Li, Y. Q.; Xu, H. B.; Huang, H. Y.; Wang, C.; Gao, L. G.; Ma, T. L. One-dimensional MoO_2-$Co_2Mo_3O_8$@C nanorods: A novel and highly efficient oxygen evolution reaction catalyst derived from metal-organic framework composites. *Chem. Commun.* **2018**, *54*, 2739–2742.

[8] Kim, K. H.; Hong, D.; Kim, M. G.; Choi, W.; Min, T.; Kim, Y. M.; Choi, Y. H. Improving electrocatalytic activity of MoO_3 for the oxygen evolution reaction by incorporation of Li ions. *ACS Mater. Lett.* **2023**, *5*, 1196–1201.

[9] Chen, Y.; Liu, Y. D.; Li, L.; Sakthivel, T.; Guo, Z. X.; Dai, Z. F. Intensifying the supported ruthenium metallic bond to boost the interfacial hydrogen spillover toward pH-universal hydrogen evolution catalysis. *Adv. Funct. Mater.* **2024**, *34*, 2401452.

[10] Lai, B.; Singh, S. C.; Bindra, J. K.; Saraj, C. S.; Shukla, A.; Yadav, T. P.; Wu, W.; McGill, S. A.; Dalal, N. S.; Srivastava, A. et al. Hydrogen evolution reaction from bare and surface-functionalized few-layered MoS_2 nanosheets in acidic and alkaline electrolytes. *Mater. Today Chem.* **2019**, *14*, 100207.

[11] Duraisamy, S.; Ganguly, A.; Sharma, P. K.; Benson, J.; Davis, J.; Papakonstantinou, P. One-step hydrothermal synthesis of phase-engineered MoS_2/MoO_3 electrocatalysts for hydrogen evolution reaction. *ACS Appl. Nano Mater.* **2021**, *4*, 2642–2656.

[12] Julien, C.; Khelfa, A.; Hussain, O. M.; Nazri, G. A. Synthesis and characterization of flash-evaporated MoO_3 thin films. *J. Cryst. Growth* **1995**, *156*, 235–244.

[13] Guo, Y. Z.; Robertson, J. Origin of the high work function and high conductivity of MoO_3. *Appl. Phys. Lett.* **2014**, *105*, 222110.

[14] Kodan, N.; Singh, A. P.; Vandichel, M.; Wickman, B.; Mehta, B. R. Favourable band edge alignment and increased visible light absorption in β-MoO_3/α-MoO_3 oxide heterojunction for enhanced photoelectrochemical performance. *Int. J. Hydrogen Energy* **2018**, *43*, 15773–15783.

[15] Omeiza, L. A.; Abdalla, A. M.; Wei, B.; Dhanasekaran, A.; Subramanian, Y.; Afroze, S.; Reza, M. S.; Bakar, S. A.; Azad, A. K. Nanostructured electrocatalysts for advanced applications in fuel cells. *Energies* **2023**, *16*, 1876.

[16] Chithambararaj, A.; Bose, A. C. Hydrothermal synthesis of

hexagonal and orthorhombic MoO_3 nanoparticles. *J. Alloys Compd.* **2011**, *509*, 8105–8110.
[17] Cai, L. L.; Rao, P. M.; Zheng, X. L. Morphology-controlled flame synthesis of single, branched, and flower-like α-MoO_3 nanobelt arrays. *Nano Lett.* **2011**, *11*, 872–877.
[18] Lupan, O.; Cretu, V.; Deng, M.; Gedamu, D.; Paulowicz, I.; Kaps, S.; Mishra, Y. K.; Polonskyi, O.; Zamponi, C.; Kienle, L. et al. Versatile growth of freestanding orthorhombic α-molybdenum trioxide nano- and microstructures by rapid thermal processing for gas nanosensors. *J. Phys. Chem. C* **2014**, *118*, 15068–15078.
[19] Chen, Y. P.; Lu, C. L.; Xu, L.; Ma, Y.; Hou, W. H.; Zhu, J. J. Single-crystalline orthorhombic molybdenum oxide nanobelts: Synthesis and photocatalytic properties. *CrystEngComm* **2010**, *12*, 3740.
[20] Xu, H. P.; Liu, C. H.; Srinivasakannan, C.; Chen, M. H.; Wang, Q.; Li, L. B.; Dai, Y. Hydrothermal synthesis of one-dimensional α-MoO_3 nanomaterials and its unique sensing mechanism for ethanol. *Arabian J. Chem.* **2022**, *15*, 104083.
[21] Ding, Q.; Song, B.; Xu, P.; Jin, S. Efficient electrocatalytic and photoelectrochemical hydrogen generation using MoS_2 and related compounds. *Chem* **2016**, *1*, 699–726.
[22] Chen, G. Y.; Lu, B. C.; Cui, X. Y.; Xiao, J. R. Effects of deposition and annealing temperature on the structure and optical band gap of MoS_2 films. *Materials* **2020**, *13*, 5515.
[23] Yu, Y. F.; Nam, G. H.; He, Q. Y.; Wu, X. J.; Zhang, K.; Yang, Z. Z.; Chen, J. Z.; Ma, Q. L.; Zhao, M. T.; Liu, Z. Q. et al. High phase-purity 1T'-MoS_2-and 1T'-$MoSe_2$-layered crystals. *Nat. Chem.* **2018**, *10*, 638–643.
[24] Soni, A.; Das, P. K.; Hashmi, A. W.; Yusuf, M.; Kamyab, H.; Chelliapan, S. Challenges and opportunities of utilizing municipal solid waste as alternative building materials for sustainable development goals: A review. *Sustain. Chem. Pharm.* **2022**, *27*, 100706.
[25] Scaglia, M.; Cornelio, A.; Zanoletti, A.; La Corte, D.; Biava, G.; Alessandri, I.; Forestan, A.; Alba, C.; Depero, L. E.; Bontempi, E. Microwave-assisted recovery of spent $LiCoO_2$ battery from the corresponding black mass. *Batteries* **2023**, *9*, 536.
[26] Shen, H. C.; Yang, Z. H.; Bao, Y. X.; Xia, X. N.; Wang, D. Impact of urban mining on energy efficiency: Evidence from China. *Sustainability* **2022**, *14*, 15039.
[27] Martín-Sómer, M.; Moreno-SanSegundo, J.; Álvarez-Fernández, C.; Van Grieken, R.; Marugán, J. High-performance low-cost solar collectors for water treatment fabricated with recycled materials, open-source hardware and 3D-printing technologies. *Sci. Total Environ.* **2021**, *784*, 147119.
[28] Wang, R.; Feng, L. L.; Yang, W. R.; Zhang, Y. Y.; Zhang, Y. L.; Bai, W.; Liu, B.; Zhang, W.; Chuan, Y.; Zheng, Z. G. et al. Effect of different binders on the electrochemical performance of metal oxide anode for lithium-ion batteries. *Nanoscale Res. Lett.* **2017**, *12*, 575.
[29] Niu, S. Q.; Li, S. W.; Du, Y. C.; Han, X. J.; Xu, P. How to reliably report the overpotential of an electrocatalyst. *ACS Energy Lett.* **2020**, *5*, 1083–1087.
[30] Anantharaj, S.; Ede, S. R.; Karthick, K.; Sam Sankar, S.; Sangeetha, K.; Karthik, P. E.; Kundu, S. Precision and correctness in the evaluation of electrocatalytic water splitting: Revisiting activity parameters with a critical assessment. *Energy Environ. Sci.* **2018**, *11*, 744–771.
[31] Fattakhova, Z. A.; Zakharova, G. S. Molybdenum oxide-based composites. *Russian J. Inorg. Chem.* **2022**, *67*, 2090–2098.
[32] Nardello, V.; Marko, J.; Vermeersch, G.; Aubry, J. M. ^{90}Mo NMR and kinetic studies of peroxomolybdic intermediates involved in the catalytic disproportionation of hydrogen peroxide by molybdate ions. *Inorg. Chem.* **1995**, *34*, 4950–4957.
[33] Segawa, K.; Ooga, K.; Kurusu, Y. Molybdenum peroxo complex. Structure and thermal behavior. *Bull. Chem. Soc. Jpn* **1984**, *57*, 2721–2724.
[34] Xia, X. B.; Guan, W. J.; Zhang, G. Q.; Zhou, Q.; Li, Q. G.; Cao, Z. Y.; Zeng, L.; Wu, S. X. Formation and stability of molybdenum and tungsten species in peroxy solution. *J. Solution Chem.* **2023**, *52*, 551–569.
[35] Guan, X.; Ren, Y. B.; Chen, S. F.; Yan, J. F.; Wang, G.; Zhao, H. Y.; Zhao, W.; Zhang, Z. Y.; Deng, Z. H.; Zhang, Y. Y. et al. Charge separation and strong adsorption-enhanced MoO_3 visible light photocatalytic performance. *J. Mater. Sci.* **2020**, *55*, 5808–5822.
[36] De Melo, O.; González, Y.; Climent-Font, A.; Galán, P.; Ruediger, A.; Sánchez, M.; Calvo-Mola, C.; Santana, G.; Torres-Costa, V. Optical and electrical properties of MoO_2 and MoO_3 thin films prepared from the chemically driven isothermal close space vapor transport technique. *J. Phys.: Condens. Matter* **2019**, *31*, 295703.
[37] Yang, J.; Xiao, X.; Chen, P.; Zhu, K.; Cheng, K.; Ye, K.; Wang, G. L.; Cao, D. X.; Yan, J. Creating oxygen-vacancies in MoO_3-nanobelts toward high volumetric energy-density asymmetric supercapacitors with long lifespan. *Nano Energy* **2019**, *58*, 455–465.
[38] Tauc, J. *Amorphous and Liquid Semiconductors*; Springer: Boston, 1974.
[39] Muralikrishna, S.; Manjunath, K.; Samrat, D.; Reddy, V.; Ramakrishnappa, T.; Nagaraju, D. H. Hydrothermal synthesis of 2D MoS_2 nanosheets for electrocatalytic hydrogen evolution reaction. *RSC Adv.* **2015**, *5*, 89389–89396.
[40] Yang, L.; Cui, X. D.; Zhang, J. Y.; Wang, K.; Shen, M.; Zeng, S. S.; Dayeh, S. A.; Feng, L.; Xiang, B. Lattice strain effects on the optical properties of MoS_2 nanosheets. *Sci. Rep.* **2014**, *4*, 5649.
[41] Joensen, P.; Crozier, E. D.; Alberding, N.; Frindt, R. F. A study of single-layer and restacked MoS_2 by X-ray diffraction and X-ray absorption spectroscopy. *J. Phys. C: Solid State Phys.* **1987**, *20*, 4043–4053.
[42] Xie, J. F.; Zhang, H.; Li, S.; Wang, R. X.; Sun, X.; Zhou, M.; Zhou, J. F.; Lou, X. W.; Xie, Y. Defect-rich MoS_2 ultrathin nanosheets with additional active edge sites for enhanced electrocatalytic hydrogen evolution. *Adv. Mater.* **2013**, *25*, 5807–5813.
[43] Liu, M. Q.; Wang, J. A.; Klysubun, W.; Wang, G. G.; Sattayaporn, S.; Li, F.; Cai, Y. W.; Zhang, F. C.; Yu, J.; Yang, Y. Interfacial electronic structure engineering on molybdenum sulfide for robust dual-pH hydrogen evolution. *Nat. Commun.* **2021**, *12*, 5260.
[44] Li, X. H.; Guo, S. H.; Su, J.; Ren, X. G.; Fang, Z. Y. Efficient Raman enhancement in molybdenum disulfide by tuning the interlayer spacing. *ACS Appl. Mater. Interfaces* **2020**, *12*, 28474–28483.
[45] Seguin, L.; Figlarz, M.; Cavagnat, R.; Lassègues, J. C. Infrared and Raman spectra of MoO_3 molybdenum trioxides and $MoO_3{\cdot}xH_2O$ molybdenum trioxide hydrates. *Spectrochim. Acta A: Mol. Biomol. Spectrosc.* **1995**, *51*, 1323–1344.
[46] Veprek, S.; Sarott, F. A.; Iqbal, Z. Effect of grain boundaries on the Raman spectra, optical absorption, and elastic light scattering in nanometer-sized crystalline silicon. *Phys. Rev. B* **1987**, *36*, 3344–3350.
[47] Shinagawa, T.; Garcia-Esparza, A. T.; Takanabe, K. Insight on Tafel slopes from a microkinetic analysis of aqueous electrocatalysis for energy conversion. *Sci. Rep.* **2015**, *5*, 13801.
[48] Kibsgaard, J.; Chorkendorff, I. Considerations for the scaling-up of water splitting catalysts. *Nat. Energy* **2019**, *4*, 430–433.
[49] Mineo, G.; Bruno, L.; Bruno, E.; Mirabella, S. WO_3 nanorods decorated with very small amount of Pt for effective hydrogen evolution reaction. *Nanomaterials* **2023**, *13*, 1071.
[50] Zhang, M.; Li, R. Q.; Hu, D.; Huang, X. F.; Liu, Y. Q.; Yan, K. Porous molybdenum trioxide as a bifunctional electrocatalyst for oxygen and hydrogen evolution. *J. Electroanal. Chem.* **2019**, *836*, 102–106.
[51] Wang, Y.; Lu, F.; Su, K.; Zhang, N.; Zhang, Y. H.; Wang, M.; Wang, X. Engineering Mo–O–C interface in MoS_2@rGO via charge transfer boosts hydrogen evolution. *Chem. Eng. J.* **2020**, *399*, 126018.
[52] Liu, Y. D.; Li, L.; Wang, L.; Li, N.; Zhao, X. X.; Chen, Y.; Sakthivel, T.; Dai, Z. F. Janus electronic state of supported iridium nanoclusters for sustainable alkaline water electrolysis. *Nat. Commun.* **2024**, *15*, 2851.
[53] Chen, Y.; Liu, Y. D.; Li, L.; Sakthive, T.; Guo, Z. X.; Dai, Z. F. Asymmetric bond delta-polarization at the interfacial Se–Ru–O bridge for efficient pH-robust water electrolysis. *Adv. Funct. Mater.*, in press, DOI: 10.1002/adfm.202406587.